Title	Three-dimensional depth-resolved and extended-resolution micro-particle characterization by holographic light scattering spectroscopy
Author(s)	Gutzler, Thomas; Hillman, Timothy R.; Alexandrov, Sergey; Sampson, David D.
Publication Date	2010
Publication Information	Gutzler, Thomas, Hillman, Timothy R., Alexandrov, Sergey A., & Sampson, David D. (2010). Three-dimensional depth-resolved and extended-resolution micro-particle characterization by holographic light scattering spectroscopy. Optics Express, 18(24), 25116-25126. doi: 10.1364/OE.18.025116
Publisher	Optica
Link to publisher's version	https://doi.org/10.1364/OE.18.025116
Item record	http://hdl.handle.net/10379/17117
DOI	http://dx.doi.org/10.1364/OE.18.025116

Three-dimensional depth-resolved and extended-resolution micro-particle characterization by holographic light scattering spectroscopy

Thomas Gutzler,[1,*] Timothy R. Hillman,[1,2] Sergey A. Alexandrov,[1] and David D. Sampson,[1,3]

[1]*Optical + Biomedical Engineering Laboratory (OBEL), School of Electrical, Electronic & Computer Engineering, M018, The University of Western Australia, 35 Stirling Highway, Crawley, Western Australia 6009, Australia*
[2]*Current address: George R. Harrison Spectroscopy Laboratory, Massachusetts Institute of Technology, 77 Massachusetts Ave., Cambridge, Massachusetts 02139, USA*
[3]*Centre for Microscopy, Characterisation & Analysis, The University of Western Australia, 35 Stirling Highway, Crawley, Western Australia 6009, Australia*
**tgutzler@ee.uwa.edu.au*

Abstract: Fourier-holographic light scattering spectroscopy is applied to record complex angular scattering spectra of two- and three-dimensional samples over a wide field of view. We introduce a computational depth sectioning technique and, for the first time, demonstrate that a single-exposure hologram can generate a quantitative, three-dimensional map of particle sizes and locations over several cubic millimeters with micrometer resolution. Such spatially resolved maps of particle sizes are generated by Mie-inversion and could not be ascertained from the directly reconstructed intensity-distribution images. We also demonstrate synthesis of multiple angular scattering intensity spectra to increase the angular range and improve size detection sensitivity.

OCIS codes: (070.0070) Fourier optics and signal processing; (090.0090) Holography; (100.2000) Digital image processing; (100.6890) Three-dimensional image processing; (120.3890) Medical optics instrumentation; (170.1650) Coherence imaging; (170.3880) Medical and biological imaging.

References and links

1. G. Sluder, and D. E. Wolf, *Digital Microscopy: a Second Edition of Video Microscopy*, (Elsevier Academic Press, Amsterdam, 2003).
2. S. A. Alexandrov, T. R. Hillman, and D. D. Sampson, "Spatially resolved Fourier holographic light scattering angular spectroscopy," Opt. Lett. **30**(24), 3305–3307 (2005).
3. T. R. Hillman, S. A. Alexandrov, T. Gutzler, and D. D. Sampson, "Microscopic particle discrimination using spatially-resolved Fourier-holographic light scattering angular spectroscopy," Opt. Express **14**(23), 11088–11102 (2006).
4. K. Sokolov, R. Drezek, K. Gossage, and R. Richards-Kortum, "Reflectance spectroscopy with polarized light: is it sensitive to cellular and nuclear morphology," Opt. Express **5**(13), 302–317 (1999).
5. V. Backman, M. B. Wallace, L. T. Perelman, J. T. Arendt, R. Gurjar, M. G. Müller, Q. Zhang, G. Zonios, E. Kline, J. A. McGilligan, S. Shapshay, T. Valdez, K. Badizadegan, J. M. Crawford, M. Fitzmaurice, S. Kabani, H. S. Levin, M. Seiler, R. R. Dasari, I. Itzkan, J. Van Dam, M. S. Feld, and T. McGillican, "Detection of preinvasive cancer cells," Nature **406**(6791), 35–36 (2000).
6. A. Wax, C. H. Yang, M. G. Müller, R. Nines, C. W. Boone, V. E. Steele, G. D. Stoner, R. R. Dasari, and M. S. Feld, "In situ detection of neoplastic transformation and chemopreventive effects in rat esophagus epithelium using angle-resolved low-coherence interferometry," Cancer Res. **63**(13), 3556–3559 (2003).
7. W. P. Van De Merwe, J. Czégé, M. E. Milham, and B. V. Bronk, "Rapid optically based measurements of diameter and length for spherical or rod-shaped bacteria in vivo," Appl. Opt. **43**(28), 5295–5302 (2004).
8. H. F. Ding, Z. Wang, F. Nguyen, S. A. Boppart, and G. Popescu, "Fourier transform light scattering of inhomogeneous and dynamic structures," Phys. Rev. Lett. **101**(23), 238102 (2008).
9. J. R. Mourant, T. M. Johnson, S. Carpenter, A. Guerra, T. Aida, and J. P. Freyer, "Polarized angular dependent spectroscopy of epithelial cells and epithelial cell nuclei to determine the size scale of scattering structures," J. Biomed. Opt. **7**(3), 378–387 (2002).
10. J. D. Wilson, and T. H. Foster, "Mie theory interpretations of light scattering from intact cells," Opt. Lett. **30**(18), 2442–2444 (2005).

#132977 - $15.00 USD Received 5 Aug 2010; revised 2 Nov 2010; accepted 5 Nov 2010; published 17 Nov 2010

11. M. J. Berg, S. C. Hill, G. Videen, and K. P. Gurton, "Spatial filtering technique to image and measure two-dimensional near-forward scattering from single particles," Opt. Express **18**(9), 9486–9495 (2010).
12. Y. Z. Zhu, M. G. Giacomelli, and A. Wax, "Fiber-optic interferometric two-dimensional scattering-measurement system," Opt. Lett. **35**(10), 1641–1643 (2010).
13. H. Fang, M. Ollero, E. Vitkin, L. M. Kimerer, P. B. Cipolloni, M. M. Zaman, S. D. Freedman, I. J. Bigio, I. Itzkan, E. B. Hanlon, and L. T. Perelman, "Noninvasive sizing of subcellular organelles with light scattering spectroscopy," IEEE J. Sel. Top. Quantum Electron. **9**(2), 267–276 (2003).
14. R. S. Gurjar, V. Backman, L. T. Perelman, I. Georgakoudi, K. Badizadegan, I. Itzkan, R. R. Dasari, and M. S. Feld, "Imaging human epithelial properties with polarized light-scattering spectroscopy," Nat. Med. **7**(11), 1245–1248 (2001).
15. Y. L. Kim, Y. Liu, R. K. Wali, H. K. Roy, M. J. Goldberg, A. K. Kromin, K. Chen, and V. Backman, "Simultaneous measurement of angular and spectral properties of light scattering for characterization of tissue microarchitecture and its alteration in early precancer," IEEE J. Sel. Top. Quantum Electron. **9**(2), 243–256 (2003).
16. R. N. Graf, and A. Wax, "Nuclear morphology measurements using Fourier domain low coherence interferometry," Opt. Express **13**(12), 4693–4698 (2005).
17. A. Wax, C. H. Yang, R. R. Dasari, and M. S. Feld, "Measurement of angular distributions by use of low-coherence interferometry for light-scattering spectroscopy," Opt. Lett. **26**(6), 322–324 (2001).
18. M. Bartlett, G. Huang, L. Larcom, and H. B. Jiang, "Measurement of particle size distribution in mammalian cells in vitro by use of polarized light spectroscopy," Appl. Opt. **43**(6), 1296–1307 (2004).
19. Y. Liu, Y. L. Kim, X. Li, and V. Backman, "Investigation of depth selectivity of polarization gating for tissue characterization," Opt. Express **13**(2), 601–611 (2005).
20. F. C. Cheong, K. Xiao, and D. G. Grier, "Technical note: characterizing individual milk fat globules with holographic video microscopy," J. Dairy Sci. **92**(1), 95–99 (2009).
21. S. Seo, T. W. Su, D. K. Tseng, A. Erlinger, and A. Ozcan, "Lensfree holographic imaging for on-chip cytometry and diagnostics," Lab Chip **9**(6), 777–787 (2009).
22. X. C. Wu, G. Gréhan, S. Meunier-Guttin-Cluzel, L. H. Chen, and K. F. Cen, "Sizing of particles smaller than 5 microm in digital holographic microscopy," Opt. Lett. **34**(6), 857–859 (2009).
23. S. H. Lee, Y. Roichman, G. R. Yi, S. H. Kim, S. M. Yang, A. van Blaaderen, P. van Oostrum, and D. G. Grier, "Characterizing and tracking single colloidal particles with video holographic microscopy," Opt. Express **15**(26), 18275–18282 (2007).
24. T. R. Hillman, T. Gutzler, S. A. Alexandrov, and D. D. Sampson, "High-resolution, wide-field object reconstruction with synthetic aperture Fourier holographic optical microscopy," Opt. Express **17**(10), 7873–7892 (2009).
25. D. J. Brady, K. Choi, D. L. Marks, R. Horisaki, and S. Lim, "Compressive holography," Opt. Express **17**(15), 13040–13049 (2009).
26. S. A. Alexandrov, T. R. Hillman, T. Gutzler, and D. D. Sampson, "Synthetic aperture fourier holographic optical microscopy," Phys. Rev. Lett. **97**(16), 168102 (2006).
27. T. Gutzler, T. R. Hillman, S. A. Alexandrov, and D. D. Sampson, "Coherent aperture-synthesis, wide-field, high-resolution holographic microscopy of biological tissue," Opt. Lett. **35**(8), 1136–1138 (2010).
28. J. W. Goodman, *Introduction to Fourier optics*, 2nd ed. (McGraw-Hill, New York, 1996).
29. I. Moon, M. Daneshpanah, B. Javidi, and A. Stern, "Automated three-dimensional identification and tracking of micro/nanobiological organisms by computational holographic microscopy," Proc. IEEE **97**(6), 990–1010 (2009).
30. B. Dai, X. D. Luo, and Y. W. Wang, "Multiple light scattering of non-spherical particles with elliptical cross section," Acta Phys. Sin. **58**, 3864–3869 (2009).

1. Introduction

The accurate determination of microscopic particle sizes is a common problem in biology. Standard characterization involves counting cells and measuring their size distribution. This task can be laborious if the use of advanced instruments, such as flow cytometers, is not feasible, because the samples must be inspected in a specific environment or even *in situ*. Histological analysis is often used to investigate the cellular composition of tissue sections [1], a time-consuming procedure for samples with large areas or a high concentration of particles. Dynamic samples are very difficult to analyze effectively using scanning imaging techniques, which usually limit collection of information to two dimensions, most commonly the surface, or have long acquisition times over which the particles are not stationary.

We have previously demonstrated a low-resolution holographic imaging technique capable of performing structural characterization of large-field-of-view samples [2,3] by comparing the angular distribution of elastic light scattering to Mie-theory predictions. Since the particle sizes were calculated from the scattering spectra, sensitivity was higher than could have been achieved by inspecting the directly resolved image. The recorded complex wave-field of each

#132977 - $15.00 USD Received 5 Aug 2010; revised 2 Nov 2010; accepted 5 Nov 2010; published 17 Nov 2010

hologram enabled us to generate fully spatially-resolved two-dimensional (2D) size maps of the samples; a single hologram provided sufficient data to analyze a millimeter-scale sample.

Using the angular light scattering spectrum to characterize particles based on Mie theory is a well-known method and has been applied to investigate dysplastic or cancerous tissue *in vivo* [4–6], bacteria [7], red blood cells [3,8] and other human cells [9,10]. Simultaneous, real-time visualization of particles and their two-dimensional forward scattering spectrum has been demonstrated [11], as has two-dimensional fiber-based measurement of the angular scattering spectrum [12]. A related, less common approach is the combination of wavelength-dependent scattering spectroscopy and Mie theory [13–15]. The particular advantage of our technique [3] is its ability to form a wide-field image, permitting a correspondence to be made between particle size and position. Extending beyond two dimensions, some techniques provide for depth sectioning via low-coherence imaging [6,16,17] or polarization gating [12,18,19].

Holography is only rarely combined with scattering spectroscopy [2,3,8,20–22], even though it offers valuable advantages over conventional light scattering spectroscopy due to its access to the complex wave-field. The possibility of computationally switching between the spectral and the spatial domain enables simultaneous reconstruction of the sample image from the spectral data. Access to the phase information within the recorded wave-field distribution permits three-dimensional (3D) digital focusing using a single hologram, enabling tracking and sizing particles at the same time, which has been demonstrated over a $3 \times 4 \times 15$ µm volume [23]. As we shall show, it also lends itself to 3D imaging enabling quantification of scatterer size and location.

In this paper, we present two techniques related to our previous work. Firstly, we extend the analysis of scattering spectra to three dimensions by performing depth sectioning via thresholding to eliminate unwanted signal from out-of-focus layers. This allows quantitative investigation of large three-dimensional volumes with a single exposure. Ours or similar techniques have not previously demonstrated such an extension. Secondly, we introduce synthetic aperture angular scattering holography (SASH), a technique to increase the collected angular scattering range by synthesizing scattering spectra recorded at different polar illumination angles. This permits the quantitative characterization of particles below the spatial and spectral resolution limit of the optical system and improves size determination sensitivity. The same low-numerical aperture optical setup is used for both experiments, permitting a large, millimeter-scale field of view and a long working distance.

2. Theory and methods

A comprehensive description of the related theoretical background is given in our previous publications [3,24]. This section extends our existing framework.

Digital refocusing of holograms is a well known technique. It has been demonstrated [25] that one hologram of a sparse three-dimensional distribution of objects contains sufficient information to reconstruct multiple, seemingly uncorrelated, slices through the volume, which overlap in the *x*-*y* plane (normal to the optical axis) but are separated in the *z*-direction (along the optical axis). This is due to the fact that if small, structured objects are well out of focus, their effect upon the reconstructed image is only a negligibly small contribution to the background.

The object's scattering intensity spectrum can be observed in the back focal (Fourier) plane of the objective lens. Figure 1 illustrates the generation of the two-dimensional scattering spectrum from light originating from two separated layers containing different size particles. The plane wave illumination beam (red) is incident on both layers and the lens L acts as an angle-dependent band-pass filter for the scattered wave-field, generating a one-to-one map between scattering angle and spatial position in the detection plane. The two-dimensional interference pattern (hologram) on the CCD sensor is a result of the superposition of the collimated wave-fields scattered from Layers 1 and 2, represented by green and blue curves, respectively, and an off-axis reference beam, which is not shown in the schematic. The visible stripes do not correspond to interference fringes but to the intensity variations of the Mie scattering spectrum.

#132977 - $15.00 USD Received 5 Aug 2010; revised 2 Nov 2010; accepted 5 Nov 2010; published 17 Nov 2010

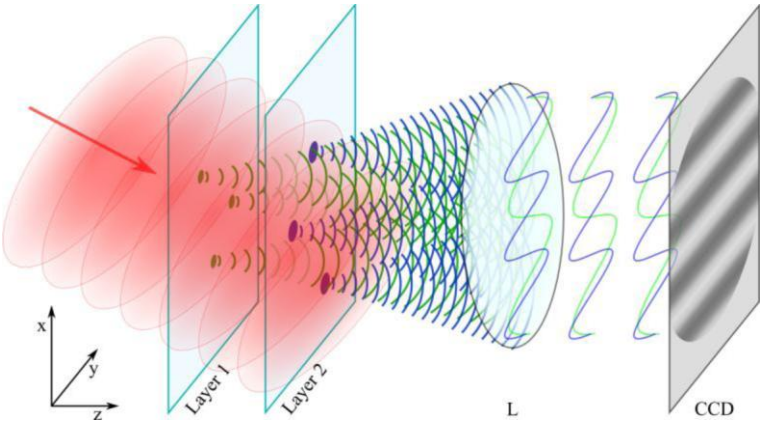

Fig. 1. Generation of angular scattering spectrum for two different scatterer sizes in two layers. The lens L generates a one-to-one map between scattering angle (sample plane) and spatial position (detection plane) and its solid angle limits the range of captured angles. The spectrum is recorded with a CCD camera. The two-dimensional intensity distribution on the detector is a result of the complex addition of scattered wave fronts from layer 1 (green), layer 2 (blue) and the reference wave (not shown).

We developed a digital filter for manipulating the hologram in order to eliminate out-of-plane information. For example, if Layer 2 is under investigation, the digital filter is equivalent to inserting multiple beam-blocks the size of a single particle into the beam path after Layer 1, blocking only light scattered by out-of-focus objects (green) and reducing the remaining light to that scattered by the particles of interest (blue). To realize this filter, we first calculate a 'contrast curve' by stepping through the volume along the optical axis and recording the ratio of standard deviation to mean intensity (contrast) for each reconstructed 2D *x*-*y* slice. We automatically detect the positions of planes containing scattering particles through sharp local maxima in the contrast curve. One of these is chosen as a "layer of interest," and we note its depth. Then, we focus to other depth planes in the sample that contain unwanted sources of scattering and set the complex-amplitude field values to zero for (*x*, *y*) positions at which the absolute value exceeds a specified threshold. After refocusing to the original depth of the scattering particles, not only a reduction of background noise in the reconstruction can be observed, but also, and more importantly, an improvement in the fidelity of the scattering spectrum. This procedure can be repeated for any depth of interest in a 3D sample.

We now consider how to determine the particle size. Due to the trade-off between field of view and numerical aperture (NA), the solid collection angle of a standard microscope objective with a millimeter-scale field of view is limited to a few degrees. In a recording medium of refractive index n_1 (generally air, $n_1 = 1$), the range of collected scattering angles is given by $\Delta\theta = 2\arcsin(\mathrm{NA}\cdot n_1 / n_{\mathrm{med}})$, where n_{med} is the refractive index of the medium surrounding the particles. Following Mie theory, we can show [3] that the average frequency of the lobes (f) in a particle's angular scattering spectrum mainly depends on its diameter (d) and increases almost linearly with the diameter, as shown in Fig. 2(a).

#132977 - $15.00 USD Received 5 Aug 2010; revised 2 Nov 2010; accepted 5 Nov 2010; published 17 Nov 2010

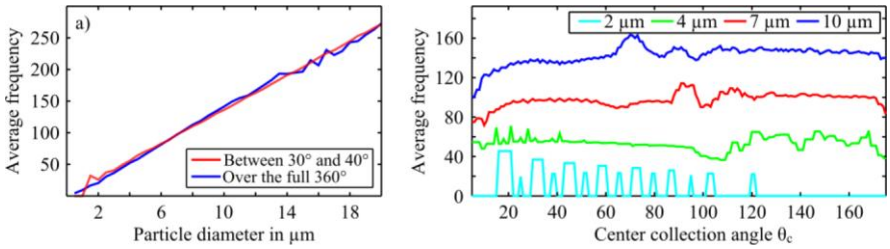

Fig. 2. Dependency of average Mie-lobe frequencies on: (a) Particle diameter; and (b) Center collection angle. Data is based on refractive indices n_{part} = 1.59 and n_{med} = 1.42.

The variation of the average lobe frequency (for a limited, off-axis, angular range,10°) as the center collection angle is varied is small [Fig. 2(b)]. Thus, particle diameter can be inferred based on determining the angular width of a single 'oscillation' (peak to peak) of the Mie spectrum, reducing the problem of size determination from complicated curve shape matching to the determination of (local) lobe frequency. This creates a hard lower limit at which the calculation of diameters for small particles based on the spectral distribution becomes impossible for a given NA. The limit is reached when the extent of a single oscillation is larger than the collection window $\Delta\theta$. In other words, the minimum detectable Mie-lobe frequency is $f_{\min} = N \cdot 2\pi/\Delta\theta$, where the scaling parameter N = 1. However, in practice, it is beneficial to ensure that either two peaks or two troughs of the oscillation pattern are contained within the collection window. Thus, the window must be enlarged by a factor of N = 1.5. The choice of parameter N = 1 guarantees only that at least one peak and one trough may be found within the window. The turquoise curve in Fig. 2(b) illustrates a case where the $f_{\min}$ condition is violated even for this value. We used Mie-theory to generate an approximate empirical formula describing the dependency of the minimum detectable particle diameter $d_{\min}$ on the system's numerical aperture NA, the refractive index of the particle-surrounding medium n_{med} and the illumination wavelength λ:

$$d_{\min} = \frac{N\pi}{\arcsin\left(\frac{\mathrm{NA}}{n_{\mathrm{med}}}\right)\cdot\left(46.3\lambda^2 - 79.5\lambda + 44.5\right)}, \qquad (1)$$

where $d_{\min}$ and λ are given in µm. This formula is valid over the ranges 0.5 µm ≤ d ≤ 20 µm, 400 nm ≤ λ ≤ 750 nm, $1.05 \le n_{part}/n_{med} \le 1.15$, where n_{part} is the particle refractive index, with a maximum error of around 10% .

A successful determination of particle size smaller than $d_{\min}$ using this technique can only be achieved by extending the solid angle of collection, that is, by increasing the numerical aperture of the objective lens. For commercial microscope objectives, this usually means decreasing the field of view as well as the working distance – two major drawbacks that we seek to avoid. We have recently reported a technique to computationally increase the numerical aperture of a holographic microscopy system [24,26,27] by recording at different illumination conditions. Here, we demonstrate a similar approach in which we sequentially record holograms at different polar illumination angles allowing the collection of a larger range of scattering angles. The subsequent synthesis of the non-negative real angular intensity spectra widens the system's angular range in one dimension. Such a technique might be called synthetic aperture angular scattering holography. Unlike our recently demonstrated synthetic aperture technique [24,27], the demanding requirement to correct for systematic phase-matching errors between different recorded *complex* wave-fields is unnecessary. This is because we do not seek to generate a high-resolution image reconstruction of the sample.

#132977 - $15.00 USD Received 5 Aug 2010; revised 2 Nov 2010; accepted 5 Nov 2010; published 17 Nov 2010

The range of scattering angles θ_s collected by the optical system is determined by the illumination angle θ_i, the detection angle $|\theta_d| < \arcsin(\mathrm{NA})$ and refractive index of the sample medium n_{med}:

$$\theta_s = \theta_c - \arcsin\left(\frac{\sin\theta_d}{n_{\mathrm{med}}}\right) = \begin{cases} \arcsin\left(\frac{\sin\theta_i}{n_{\mathrm{med}}}\right) - \arcsin\left(\frac{\sin\theta_d}{n_{\mathrm{med}}}\right), 0 \le \theta_i < \frac{\pi}{2} \\ \arccos\left(\frac{\sin\theta_i}{n_{\mathrm{med}}}\right) + \arccos\left(\frac{\sin\theta_d}{n_{\mathrm{med}}}\right), \frac{\pi}{2} \le \theta_i < \pi \end{cases}, \quad (2)$$

where the upper and lower parts are valid for transmission and reflection, respectively. The angle θ_c is the center collection angle, the angle between the optical axis and the illumination beam inside the medium; the remaining three angles are depicted in Fig. 3.

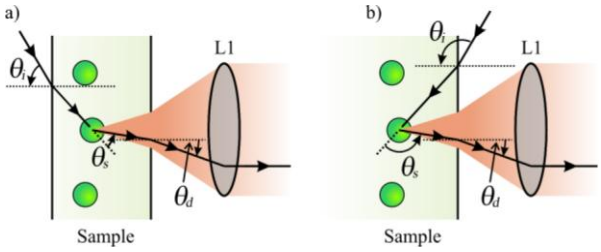

Fig. 3. Schematic diagram showing the relationship between illumination, scattering and detection angles configured for: a) Transmission; and b) Reflection scattering geometries.

Fourier holography is a suitable imaging modality for SASH as the recording-plane sample-wave intensity distribution is equal to the angular scattering spectrum averaged over the entire sample [3]. Equation (2) shows the direct dependence of the center collection angle θ_c on the illumination angle θ_i. The former determines the location of the captured angular range within the entire spectrum. By recording slightly overlapping parts of the scattering spectrum and stitching them together in post-processing, we can create the synthesized angular scattering spectra in either a reflection or a transmission geometry.

For large scattering angles, lines of equal scattering angle (but varying azimuthal angle) are approximately straight and parallel in the recording plane [3]. However, their curvature increases with decreasing scattering angle, as illustrated in Fig. 4. We accounted for this curvature during post-processing by extracting one-dimensional spectra as the mean of the contributing pixels along the curves. The limiting pupil of the system is determined by the circular objective lens aperture and the rectangular CCD sensor, as indicated in Fig. 4. The small relative contribution of the lowest and highest scattering angles to this region (a 'vignetting' effect) results in a signal-to-noise-ratio reduction for these portions of the spectrum.

#132977 - $15.00 USD Received 5 Aug 2010; revised 2 Nov 2010; accepted 5 Nov 2010; published 17 Nov 2010

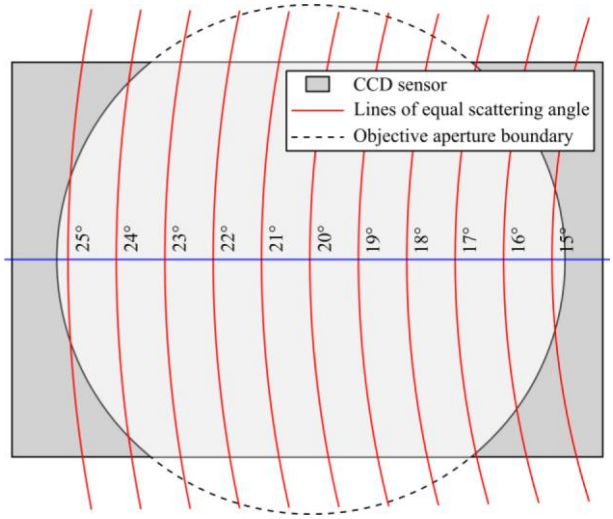

Fig. 4. Lines of equal scattering angle (red) indicate the distribution of light on the CCD sensor, including the 'vignetting' effect of the objective on the sensor with respect to the lowest and highest scattering angles.

3. Sample preparation

The samples used for both experiments are polystyrene microspheres embedded in a thin silicone layer on a standard microscope glass slide. We used a pourable, addition-curing RTV-2 silicone rubber (Wacker Silicones, Elastosil RT 601 A/B; component A contains the platinum catalyst, component B the crosslinker, n_{med} = 1.42). The microspheres (Bangs Laboratories: 2.5 µm (σ = 0.25 µm), 5.43 µm (σ = 0.14 µm), 11.44 µm (σ = 0.21 µm), with n_{part} = 1.59) were originally suspended in water at 10% weight by volume, which made the combination with the hydrophobic silicone difficult. To achieve efficient mixing, the following procedure was adopted: 6 µl of the suspension was added to 3 g of silicone (RT 601 A) and stirred for an hour at 1500 rpm until the mixture appeared homogeneous. Then, the viscosity was reduced by adding 600 µl of hexane and stirring was continued for 1 minute at 1000 rpm. After removing air bubbles from the mixture under vacuum, the suspension was placed in an ultra-sonic bath for 10 minutes to break up aggregations. To initialize the curing, the crosslinker (RT 601 B) was added at a 1:20 weight ratio and stirring was continued at 250 rpm for another 5 minutes. A droplet (~50 µl) from the resulting mixture was deposited on a cleaned microscope glass slide (25.4 × 76.2 × 0.9 mm) and covered with another glass slide until the sphere/silicone mix stopped spreading. The top glass slide was removed by pulling it sideways at constant speed, leaving a thin layer with a flat surface. The sample was placed in a dust-free oven for 12 hours until the water and hexane had evaporated and the silicone was fully cured. A two-layer sample was created by gluing two single-layer slides together back to back using UV-curable optical cement (Norland Optical Adhesive 81).

4. Experimental setup

A schematic drawing of the optical setup in transmission configuration is shown in Fig. 5. A coherent laser beam (He-Ne, λ = 632.8 nm) is split into reference and sample waves. The sample is placed in the focal plane of lens L1 (NA = 0.13, 40 mm working distance), which performs an optical Fourier transform. The sample field of view is restricted to a 3 × 3-mm area by a rectangular field stop in the image plane and passed through a polarizer before its Fourier spectrum is combined with the off-axis reference wave and their interference pattern recorded by the CCD camera (12-bit, 4008 × 2762 pixels). To avoid under/overexposure of the detector due to varying signal strength, the camera's shutter time was adjusted to use its full dynamic range and neutral density filters (ND) were used in the reference arm to maintain

#132977 - $15.00 USD Received 5 Aug 2010; revised 2 Nov 2010; accepted 5 Nov 2010; published 17 Nov 2010

an approximately constant power ratio between sample and reference arms. The sample-arm polarizer is used to select one linear polarization state of the scattered light; the reference-arm half-wave plate is used to match the two arms' polarization states. The reference-arm beam is expanded and spatially filtered by a telescope T.

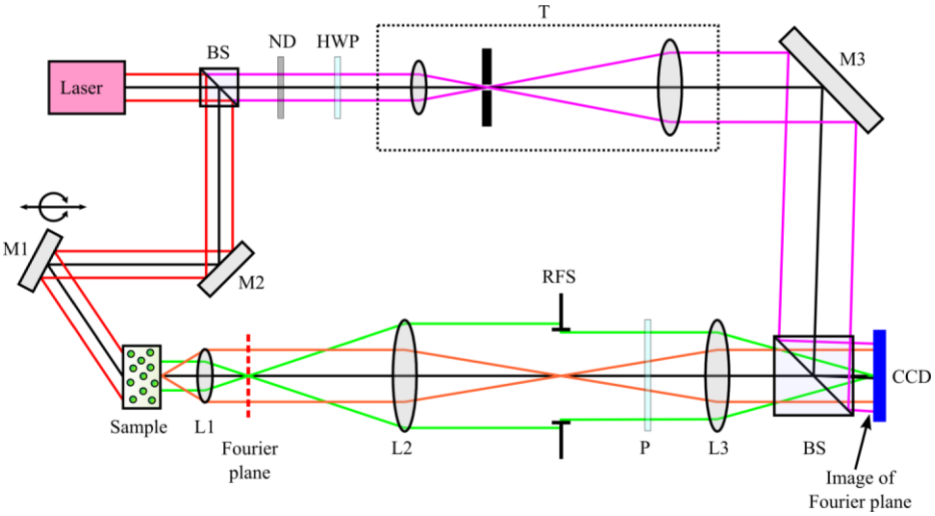

Fig. 5. Schematic diagram of the optical setup in transmission configuration. L1, L2 and L3 are lenses of the 6-f system, mirrors and beam splitters are labeled M1, 2, 3 and BS, respectively, ND is a neutral density filter, HWP and P are half-wave plate and polarizer, RFS is a rectangular field stop and T a telescopic system with spatial filter (pinhole). The imaging sensor is a charge-coupled device (CCD). Figure 3(a) shows a more detailed view of the sample area.

The sample illumination mirror M1 is mounted on a computer controlled rotation stage, which can be translated parallel to the optical axis, permitting both a transmission and reflection configuration and precise measurement of the variable incident angle θ_i. For this system, we calculated the range of captured scattering angles to be $\Delta\theta$ = 10.5°, which yields a minimum (N = 1) detectable diameter of d_{min} = 2.69 µm, according to Eq. (1). With the more conservative condition of N = 1.5, d_{min} increases to 4.03 µm.

5. Results and discussion

To demonstrate single-exposure, three-dimensional particle characterization, a two-layer sample with sphere sizes of 11.4 µm (Layer 1) and 5.4 µm (Layer 2) was used. Refocusing distances for each layer (relative to the front focal plane of the objective lens) were 0.04 mm and 1.28 mm, respectively, corresponding to a physical separation of 1.87 mm (n_{glass} = 1.51), with the thickness of each silicone layer being less than 50 µm. After the hologram was recorded, the reconstruction was divided into an 11 × 11 grid (270 × 270 µm regions) and local scattering spectra were extracted for each region at the two refocusing distances.

Figure 6(a) shows the particle sizes calculated from the 242 scattering plots without out-of-plane background suppression. The red and blue plots show similar apparent size distributions, which is explained by noting that the scattering spectrum is based on the intensity values of the Fourier transform of the complex object wave-field. Defocusing in the object plane corresponds to multiplication by a quadratic phase factor in the Fourier plane [28], an operation which does not affect the intensity distribution. That is, being "out-of-focus" does not diminish a particle's contribution to the measured angular spectrum.

#132977 - $15.00 USD Received 5 Aug 2010; revised 2 Nov 2010; accepted 5 Nov 2010; published 17 Nov 2010

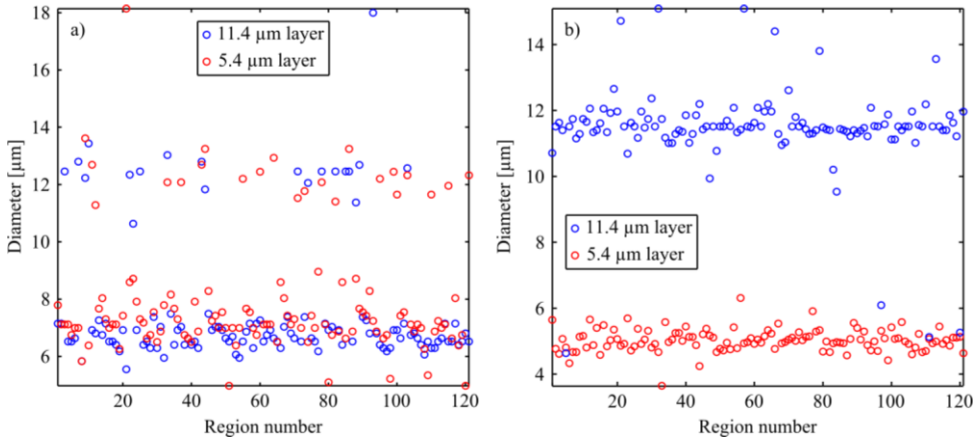

Fig. 6. Calculated particle diameters for regions of the two-layer sample: (a) Without thresholding; and (b) With thresholding.

In the next step, a binary mask was created for each of the two layers, the 'digital filter' described in Section 2. The value of a pixel in the mask is 1 if the intensity at the same coordinates in the reconstruction was below a certain threshold and 0 otherwise. The threshold t was calculated as the percentile-p reconstruction intensity value (p% of all intensity values are below t). It was found that for our experiments, p = 97 yielded the best results. To analyze Layer 1, we digitally focus on Layer 2, multiply the complex array by the mask and then focus on Layer 1. In this way, we also obtain a "cleaned-up" reconstruction. A Fourier transform yields the modified scattering spectrum. This method was repeated for the 121 individual regions and the calculated scatterer sizes are plotted in Fig. 6(b). Apart from a few outliers, the size calculation worked well and good separation of the layers is observed. Outliers usually occur when the investigated region is very close to the border of the reconstruction, where imaging artifacts are the most prevalent.

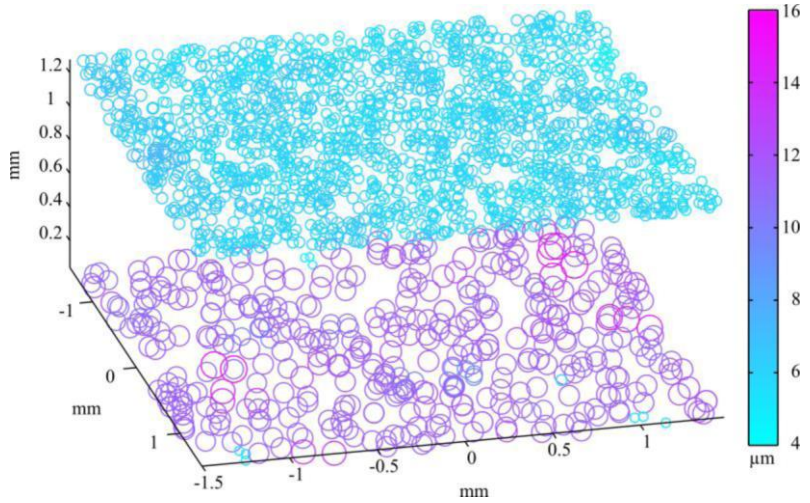

Fig. 7. Three-dimensional representation of detected sphere sizes in µm and locations in the 3 × 3 × 1.2 mm volume (displayed sphere sizes not to scale).

In addition to particle size, our algorithm is capable of detecting the location of the particles in each layer. The transverse (in-plane) location accuracy is limited by the spatial resolution of the optical system, while the depth information, which is based on the digital refocusing parameter, is limited by the depth of field of the objective lens. The latter was calculated to be approximately 40 µm and should be adequately sampled with focusing depth

#132977 - $15.00 USD Received 5 Aug 2010; revised 2 Nov 2010; accepted 5 Nov 2010; published 17 Nov 2010

increments of 20 μm. Figure 7 is the result of combining all of the collected information. A three-dimensional representation of the spheres in each layer is shown, where each detected particle is depicted as a circle. The diameter of each circle represents the particle's detected size (not to scale) and the color map acts as an additional visual indicator.

This technique is not restricted to two-layer samples and particles in layers separated by less than 40 μm will still be distinguished unless their transverse (*x*, *y*) distance is within the resolution limit. However, the particle density presents a limitation, since setting a large number of pixels to zero will inevitably have a deleterious effect on the reconstruction, even after refocusing to a different position. At the same time, the power of the scattering spectrum increases with the number of scatterers per analyzed region. The trade-off between these two parameters has not been fully characterized. In this experiment, good results were achieved with densities of approximately 4 (11.4 μm layer) and 16 (5.4 μm layer) particles per region.

To demonstrate synthetic aperture angular scattering holography, we made a sample containing a single layer of 2.5 μm spheres. Holograms were recorded whilst changing the polar angle of illumination in 6° increments between 20° and 74°. Taking the refractive index of the silicone into consideration, this corresponds to a center illumination angle range of $\theta_c = 13.9° - 42.6°$, which results in the range of accessible scattering angles $\theta_s = 8.7° - 47.9°$. Figure 8(a) shows the synthesis of ten scattering spectra recorded for different illumination angles. The individual curves represent the normalized average scattering spectrum over the entire sample. An individual curve was suboptimal for accurate particle sizing as the value of *N* was 0.93, just below the minimum required value. The curves were synthesized by scaling and shifting them along the *y* axis to compensate for the changes in the settings used (exposure time and ND filter density), to maximize the detector dynamic range. The dashed curve represents the values calculated from Mie theory for the given parameter set. A very good fit can be observed between the theoretical and measured values. Each individual spectrum shows much smaller than expected values at the ends of the scans caused by the aforementioned objective vignetting, which reduces the number of pixels illuminated by light scattered at angles very close to the cut-off.

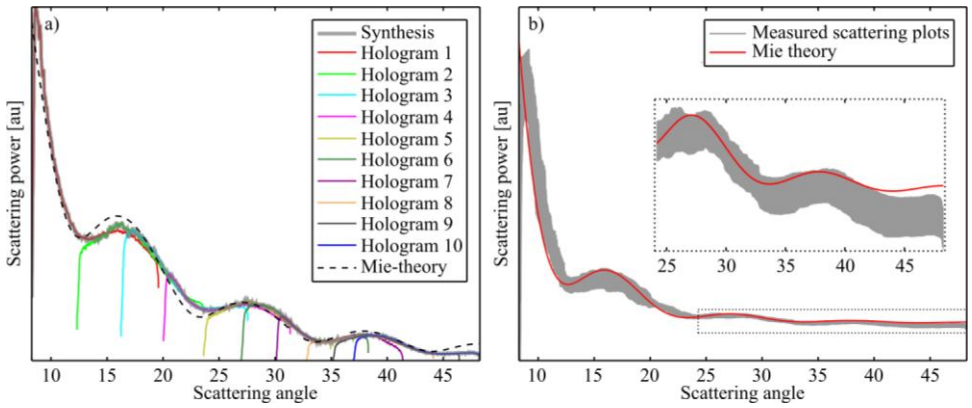

Fig. 8. Synthesis of ten angular scattering spectra of 2.5 μm spheres (hologram 1-10) and comparison to Mie theory: (a) For the entire reconstruction; and (b) For 121 sub-regions. The gray areas indicate the spread in the measured data.

Additionally, an analysis of the local scattering spectra was performed on 121 uncorrelated regions of the reconstruction; each about 270 × 270 μm in size. Synthesis of the local spectra was performed in the manner described above. The gray shaded area in Fig. 8(b) represents the upper and lower limits of all 121 synthesized spectra in comparison with the theoretical values in red. Again, a very good match between experiment and theory can be seen. The inset is a magnified version of the highlighted part of the tail of the curve. For 99% (90%) of the measured curves, the standard deviation of their individual values was below 10% (2%) of the mean. The calculation of the diameters yielded a mean value of 2.55 μm with a standard

#132977 - $15.00 USD Received 5 Aug 2010; revised 2 Nov 2010; accepted 5 Nov 2010; published 17 Nov 2010

deviation of 0.13 μm. A systematic angular offset between theory and measurement of approximately 1° can be observed. This is most likely due to a slight misalignment of the illumination mirrors, as it is apparent in all plots over all angular ranges.

Even though our experiments were performed using spherical particles, both techniques could be adapted to other particle shapes. Shape recognition [29] and size-determination algorithms for non-spherical particles [30] based on their scattered wave fronts have been demonstrated and could be applied to our technique, permitting a large variety of samples to be analyzed and characterized.

Any given hologram from a series of recordings at varying polar angles could also be analyzed with the 3D characterization algorithm to yield a particle map. Averaging over such particle maps extracted from multiple holograms recorded at different angles can potentially increase the accuracy of scatterer locations. Thus, combining synthetic aperture angular scattering holography with 3D characterization could offer a larger size measurement range at an improved sensitivity as well as a more accurate 3D location map.

A working distance of 40 mm permits imaging inside transparent containers and wells and also through glass surfaces. The rectangular field stop currently limits the field of view to a 3 × 3 mm area creating twin images of approximately 1300 × 1300 pixels in the reconstruction. Since our sensor can comfortably fit two 1300 × 2600 pixel areas, the stop could be opened up to a field of view of as large as 3 × 6 mm.

6. Conclusions

We have demonstrated two complementary holographic angular scattering spectroscopy techniques. For the first time, to our knowledge, spherical particles in a 3 × 3 × 2 mm volume were characterized with micrometer resolution, using single-exposure spatially resolved angular scattering holography. To differentiate between different layers, a thresholding technique was introduced, which we used for depth sectioning in both the image reconstruction and the scattering spectrum of the sample. In addition to biological applications, this technique could be used for the investigation of particles suspended in liquids and particle clouds.

We also successfully demonstrated the characterization of scatterers using synthetic-aperture angular scattering holography. Angular scattering spectra collected from particles smaller than the spatial resolution of the optical system could not be uniquely identified with a particle size based on a single hologram. Only by synthesizing the scattering spectra was it possible to accurately determine the size of the small spheres, making it possible to extend scattering spectroscopy techniques to quantitative wide-field imaging of micrometer-size particles.

Future work includes extending the synthetic aperture setup to simultaneously detect two or more independent wave fronts, for example, using two orthogonal polarizations or wavelength multiplexing. Both options would make possible a single-shot, synthetic-aperture version of the demonstrated technique. The combination of both techniques could provide for the differentiation of scatterers as small as 1 μm in volumes larger than 30 mm^3.

#132977 - $15.00 USD Received 5 Aug 2010; revised 2 Nov 2010; accepted 5 Nov 2010; published 17 Nov 2010